JACS JOURNAL OF THE AMERICAN CHEMICAL SOCIETY

Article

Cite This: J. Am. Chem. Soc. 2017, 139, 18681−18687

pubs.acs.org/JACS

Selective Charging Behavior in an Ionic Mixture Electrolyte-Supercapacitor System for Higher Energy and Power

Xuehang Wang,[†,‡] Aleksandar Yordanov Mehandzhiyski,[†] Bjørnar Arstad,[§] Katherine L. Van Aken,[‡] Tyler S. Mathis,[‡] Alejandro Gallegos,[¶] Ziqi Tian,[∥] Dingding Ren,[⊥] Edel Sheridan,[#] Brian Arthur Grimes,[†] De-en Jiang,[∥] Jianzhong Wu,[¶] Yury Gogotsi,*[,‡] and De Chen*[,†]

[†]Department of Chemical Engineering, Norwegian University of Science and Technology, 7491 Trondheim, Norway

[‡]Department of Materials Science and Engineering and A. J. Drexel Nanomaterials Institute, Drexel University, Philadelphia, Pennsylvania 19104, United States

[§]SINTEF Materials and Chemistry, Blindern, 0314 Oslo, Norway

[∥]Department of Chemistry, [¶]Department of Chemical and Environmental Engineering, University of California, Riverside, California 92521, United States

[⊥]Department of Electronic Systems, Norwegian University of Science and Technology, 7491 Trondheim, Norway

[#]SINTEF Materials and Chemistry, 7491 Trondheim, Norway

Supporting Information

ABSTRACT: Ion−ion interactions in supercapacitor (SC) electrolytes are considered to have significant influence over the charging process and therefore the overall performance of the SC system. Current strategies used to weaken ionic interactions can enhance the power of SCs, but consequently, the energy density will decrease due to the increased distance between adjacent electrolyte ions at the electrode surface. Herein, we report on the simultaneous enhancement of the power and energy densities of a SC using an ionic mixture electrolyte with different types of ionic interactions. Two types of cations with stronger ionic interactions can be packed in a denser arrangement in mesopores to increase the capacitance, whereas only cations with weaker ionic interactions are allowed to enter micropores without sacrificing the power density. This unique selective charging behavior in different confined porous structure was investigated by solid-state nuclear magnetic resonance experiments and further confirmed theoretically by both density functional theory and molecular dynamics simulations. Our results offer a distinct insight into pairing ionic mixture electrolytes with materials with confined porous characteristics and further propose that it is possible to control the charging process resulting in comprehensive enhancements in SC performance.

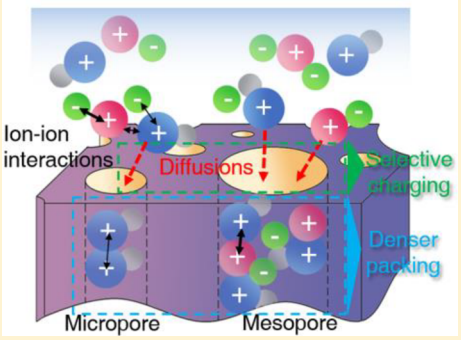

INTRODUCTION

A supercapacitor (SC) stores charge through fast and reversible ion adsorption at the electrode surface, which enables high-power output and extended cycling lifetimes.[1−3] Enhancing the energy density of SCs, while still maintaining their high-power and long life, would expand their utilization into high-energy applications. Current strategies to improve SC energy density involve the employment of both nonaqueous electrolytes[4,5] and microporous electrode materials,[3,6,7] which both can efficiently improve the energy density due to expanded voltage windows and efficient electrode surface utilization. However, ion transport resistance within the nanoporous materials dramatically increases due to the large sizes of the ions used in nonaqueous electrolytes, leading to undesired reductions of power density. Therefore, a strategy for enhancing energy density without sacrificing power density is highly sought after.

The capacitance of a SC, or more intuitively, the number of charged ions adsorbed per unit of the electrode material, is closely related to the geometric sizes of the ionic species in the electrolyte as well as the pore structure of the electrode material.[6−10] Furthermore, the actual energy and power characteristics of the SC are highly dependent on the dynamics of ion transportation.[11−15] Fundamental studies have revealed that overall ion diffusion is dominated by ion−ion interactions in two ways: (1) the electrostatic forces between the counterions and (2) steric effects caused by a large ion population in a confined space.[13,16,17] Neat ionic liquid electrolytes store charge in micropores very efficiently with almost no ion-pairing and overscreening effects, but the resistance for ion transport is large due to the relatively strong cation−anion interactions within the electrolyte.[10,18−21] The addition of a solvent is a very direct way to enhance ion diffusion by reducing the counterion attraction, but doing so will reduce the system's capacitance due

Received: October 12, 2017
Published: November 29, 2017

DOI: 10.1021/jacs.7b10693
J. Am. Chem. Soc. 2017, 139, 18681−18687

to the formation of solvation shells around the ions, which then lowers the space utilization of the porous electrode structure.[22] Utilizing micropores with pore sizes close to the ion size can avoid capacitance loss from solvation shell formation, but this approach results in a new problem in the form of large ion diffusion resistance within the micropores.[6,21−23] Another way to assist ion diffusion is to mitigate steric effects by reducing the ion population in the pores during the charging process. In theory, an ionophobic material with ion-free pores can efficiently avoid steric effects, but such a material has not yet been developed.[13,24] Different charging mechanisms (ion exchange, ion desorption and ion adsorption) take place based on the polarization of the electrode and the choice of ions, which may influence ion diffusion by changing the in-pore ion density and ion diffusion kinetics.[25] However, the causes for the different charging mechanisms remain unknown and therefore it is impossible to control the charging mechanism of SCs using current experimental methods.

In this study, we report on simultaneous enhancements in the energy and power of a SC using a multication ionic liquid mixture, namely a mixture of 1-ethyl-3-methylimidazolium ($EMIM^+$) and tetramethylammonium (TMA^+) combined with a single anion, tetrafluoroborate (BF_4^-). Our results show that only $EMIM^+$ ions, which have weaker ionic interactions, are allowed to enter micropores. This prevents the large ion diffusion resistance that would otherwise occur if TMA^+ ions were able to enter the micropores. Furthermore, we also show that TMA^+ ions are able to access the less confined spaces of mesopores together with $EMIM^+$ ions resulting in denser ion packing and enhanced capacitance. This unique selective charging behavior was directly observed by solid-state nuclear magnetic resonance (NMR) measurements, and these observations were in good agreement with theoretical calculations based on both classical Density Functional Theory (cDFT) and Molecular Dynamic (MD) simulations.

Enhanced Capacitance in a Mesopore-Rich Carbon with an Ionic Mixture Electrolyte. Reducing the ion−ion separation of the adsorbed ions on an electrode's surface efficiently increases surface area utilization, leading to enhanced capacitance.[8] Among all salts with low melting points, the smallest cation is $EMIM^+$, which is much larger compared to the selectable anions, such as BF_4^-, chloride (Cl^-) and hexafluorophosphate (PF_6^-).[27] Because the capacitance of a symmetrically assembled SC is dependent on the electrode that adsorbs the largest ion species, we will focus exclusively on modifying the behavior of large, organic cations in this study.[28] Although there are organic cations smaller than $EMIM^+$, such as TMA^+, salts with these smaller cations are solids at room temperature and cannot be used directly as the electrolyte for energy-storage applications. Dissolving $TMABF_4$ in an organic solvent is one common way to use TMA^+ salts in electrolytes, but the solvation process lowers ion packing density and results in lower capacitance. It was shown that a mixture of two ionic liquids that have a common anion but have cations with dissimilar sizes disrupts ordered ion packing and inhibits recrystallization, resulting in a decrease in the melting point of the multication ionic liquid.[29,30] Similarly, mixing the ionic liquid $EMIMBF_4$ with $TMABF_4$ also lowers the melting point of their mxiture, which results in a room temperature liquid phase ionic mixture, as shown in Figure S1.

To determine the influence that the addition of a small cation to an ionic liquid has on the performance of a SC, we used $TMABF_4$/$EMIMBF_4$ electrolytes with $TMABF_4$ concentrations ranging from 0 to 25 wt % in two-electrode symmetric SCs. Three mesoporous carbon materials prepared by carbonizing and activating polyaniline (for detailed preparation method, see Supporting Information S1.1), referred to as Meso-1.8 nm, Meso-2.0 nm and Meso-2.7 nm (numbers refer to the average pore size of the materials), were used as the electrode materials. The general morphology (Figure S2), nitrogen adsorption/desorption isotherms (Figure S3a), pore size distributions (PSDs) (Figure S4a) and pore characteristics (Table S1) are described in the Supporting Information. Galvanostatic charge/discharge (GCD) curves of the Meso-2.0 nm SC at a current density of 1 A/g are shown in Figure 1a. With increased $TMABF_4$ concentrations the charge/discharge time of the GCD curves increased while retaining the triangular shape characteristic of capacitive behavior. The capacitance, calculated from the GCD discharge time, increased from 143 to 182 F/g when the concentration of $TMABF_4$ increased from 0 to 20 wt %. The rectangular shape of the cyclic voltammograms (CVs) at a low scan rate of 10 mV/s shows no obvious distortions and good capacitive behavior for a voltage window of 3.5 V with different $TMABF_4$ concentrations (Figure 1b). The expanded area of the voltammograms is consistent with the observation from the GCD curves that capacitance increases with increasing $TMABF_4$ concentration. Similar results were obtained for Meso-1.8 nm and Meso-2.7 nm electrode materials (Figure S5). The capacitance increased further with a $TMABF_4$ concentration of 25 wt %, but there was an obvious distortion in the GCD curves, so 20 wt % was chosen as the limit for $TMABF_4$ addition. In order to quantify the capacitance increase relative to the $TMABF_4$ concentration, the capacitance at different $TMABF_4$ concentrations was normalized to the capacitance of the neat $EMIMBF_4$ electrolyte for the same electrode material ($C_{mixture}/C_{0\ wt\ \%}$). The normalized capacitance vs $TMABF_4$ concentration is shown in Figure 1c, where there is a clear trend of increased capacitance with increasing $TMABF_4$ concentration.

To understand the mechanism of the observed capacitance increase, the operating voltage window of the SC (Meso-2.0 nm) was lowered to get rid of the influence from any possible side reactions and other pesudocapacitive contributions. GCD curves with perfectly linear charge/discharge profiles were observed when the voltage was lowered to 1.5 V for electrolytes with $TMABF_4$ concentrations of 0 and 15 wt %, indicating that the charge storage mechanism is dominated by the physical adsorption of ions at the electrode surfaces (Figure S6a). The SC with 15 wt % $TMABF_4$ electrolyte showed 15% higher capacitance compared to that of the neat ionic liquid electrolyte. This means more cations per unit of surface area are adsorbed at the electrode surface following the addition of $TMABF_4$. The addition of a pseudoreference electrode was used to study the charging behavior of the positive and negative electrodes simultaneously.[4] The balance (central line) between the two electrodes shifts toward the negative electrode following the addition of $TMABF_4$ into the $EMIMBF_4$ electrolyte (Figure S6b). This is a clear indication that more cations are adsorbed on the negatively charged mesoporous carbon electrode after $TMABF_4$ is added.

Classical density functional theory (cDFT) simulations were carried out to investigate the capacitive behavior of an electrolyte with mixed cations in a carbon material with regular slit pores with pore sizes of 1.875 nm (Figure 1d; for simulation details, see Supporting Information Part S3). $EMIM^+$ ions are simplified into a charged sphere (imidazolium ring) connected to an uncharged sphere (ethyl group), whereas TMA^+

DOI: 10.1021/jacs.7b10693
J. Am. Chem. Soc. 2017, 139, 18681−18687

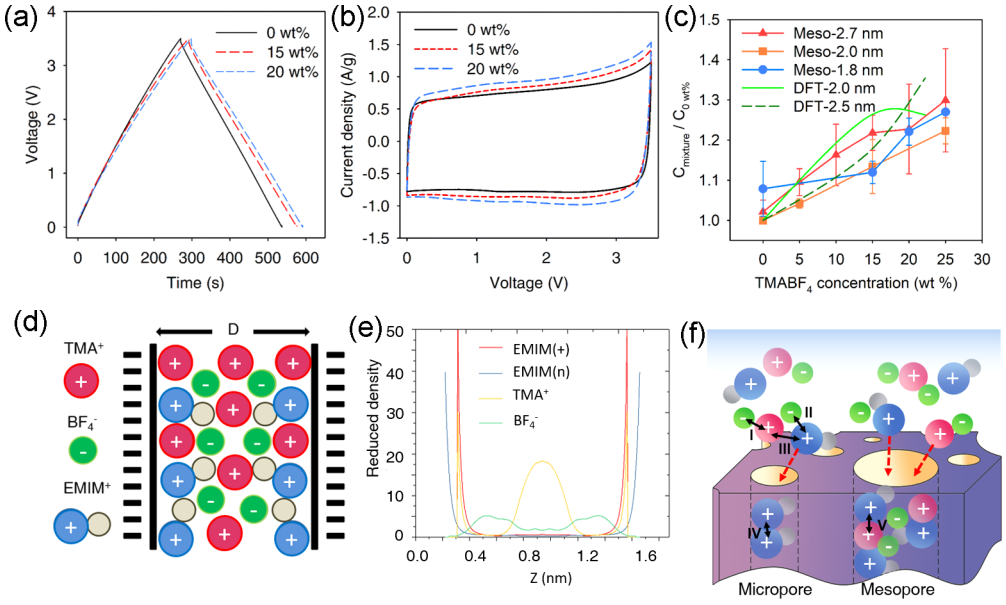

Figure 1. (a,b) GCD at 1 A/g and CV curves at 10 mV/s of the mesopore-rich carbon Meso-2.0 nm. (c) Relation between normalized capacitance and $TMABF_4$ concentration with three mesopore-rich carbon materials. (d) Schematic representation of a room-temperature ionic mixture in a charged slit pore: TMA^+ and BF_4^- ions are represented by charged hard spheres and $EMIM^+$ by a charged sphere 'EMIM(+)' in connection with a neutral sphere 'EMIM(n)' that accounts for the uncharged ethyl group, the size of the spheres is determined by the molecular volume.[26] (e) Distribution of cations and anions inside a slit pore (pore size = 1.875 nm) with negatively charged walls (ψ-PZC= −1.5 V) for the case of 22.2 wt % $TMABF_4$ in $EMIMBF_4$. (f) Schematic of the ionic interaction induced selective charging behavior of ionic mixture electrolyte. Black arrows (↔) represent ionic interactions: I. TMA^+−BF_4^- interaction; II, $EMIM^+$−BF_4^- interaction; III, steric effect near high confinement pore; IV, $EMIM^+$−$EMIM^+$ interaction; V, TMA^+−$EMIM^+$ interaction; red arrows (→) represent ion diffusion.

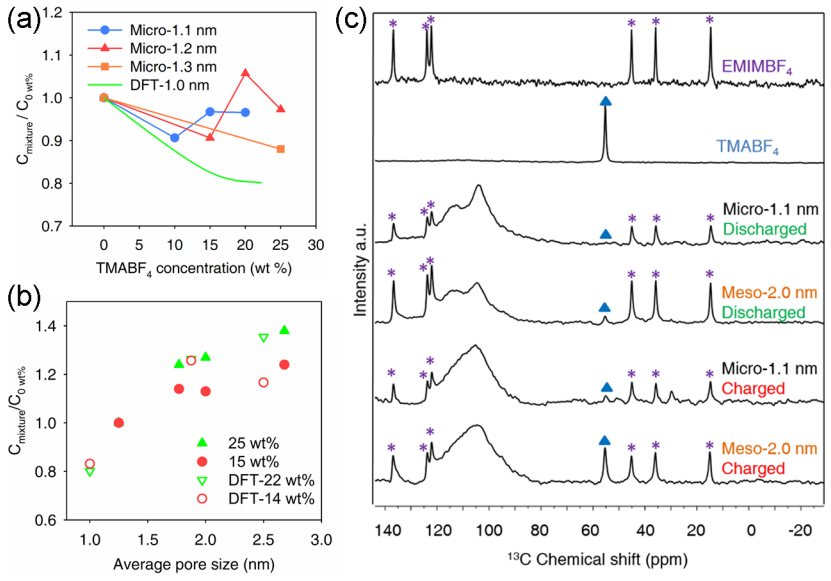

Figure 2. (a) Relation between normalized capacitance and $TMABF_4$ concentration with microporous carbon. (b) Relation between normalized capacitance and average pore sizes. (c) ^{13}C NMR spectrum of separate components of discharged and charged electrode

is represented by a single sphere. In this way, the influence from the ion size and ion orientation will be included during simulation. When all ionic interactions (carbon−ion interactions, cation−anion interactions, and cation−cation interactions) are taken into consideration, the predicted capacitances are highly consistent with the experimental results (Figure 1c). Notably, although the simulation systems are idealized, a good agreement between the simulated results and experimental observations suggests that the ionic interactions are dominant for the capacitance enhancement.

cDFT predicts that there is simultaneous adsorption of TMA^+ on the charged electrode surface with $EMIM^+$ (Figure 1e). As illustrated in Figure 1d, the charged part of $EMIM^+$ occupies similar surface area to TMA^+ on the electrode. Thus, the smaller size of TMA^+ relative to $EMIM^+$ cannot explain the enhanced capacitance in a mesoporous carbon. Interestingly, based off the simulation results, the enhanced capacitance is mainly due to the weaker cation−cation repulsion between TMA^+−$EMIM^+$ pairs than that between $EMIM^+$−$EMIM^+$ pairs. Electron-rich π-system of the imidazolium ring has a partial negative charge above and below the ring.[31,32] Hence, an electrostatic attraction will arise from the positively charged species TMA^+ and the electron-rich imidazolium ring of

DOI: 10.1021/jacs.7b10693
J. Am. Chem. Soc. 2017, 139, 18681−18687

$EMIM^+$, weakening the repulsions between TMA^+ and $EMIM^+$. It is important to note that the strength of cation−π interactions is significant, and can be of the same order as hydrogen bonds.[33] This results in the mixed TMA^+ and $EMIM^+$ cations being packed more closely than solitary $EMIM^+$ cations in the mesopores (larger attractive ionic interaction of V than IV in Figure 1f), leading to improved capacitance.

Selective Charging Behavior. For comparison to the mesoporous carbon, three different kinds of microporous carbon materials were tested as active electrode materials, specifically a Titanium carbide derived carbon (Micro-1.1 nm), a commercial activated carbon YP-50F (Micro-1.2 nm) and activated carbon spheres (Micro-1.3 nm) (numbers refer to the average pore size of materials; for general morphology, see Figure S2). For these three carbon materials, the majority of the pore volume is composed of micropores with pore size <2 nm (PSDs shown in Figure S4b). The capacitive behavior of these microporous carbons was analyzed for both the neat $EMIMBF_4$ electrolyte and the ionic mixture electrolytes (Figure S7a−d). Surprisingly, the capacitance of these microporous carbons, calculated from electrochemical measurements and cDFT simulations, does not increase monotonically with increasing $TMABF_4$ concentrations (Figure 2a), instead it varies from around 0.9 to 1.1 (normalized capacitance). To gain more insight into the differences in capacitive behavior between the mesoporous and microporous materials, the capacitance change ($C_{mixture}/C_{0\ wt\ \%}$) was plotted versus the average pore sizes of the different carbon materials (Figure 2b). Interestingly, the larger the average pore size is, the more the capacitance increases by adding $TMABF_4$. Because a larger average pore size is the result of a higher proportion of mesopores based on the PSDs (Figure S4), this suggests that the addition of $TMABF_4$ only has an impact when mesopores are present. Based on cDFT simulations, the number density of the TMA^+ ions increases in the bulk of the electrolyte and in mesopores with increasing $TMABF_4$ concentration, while there are negligible changes in micropores (Figure S8a,b). Hence, the selective entrance of TMA^+ into the mesopores leads to a capacitance enhancement in mesopore-rich carbon compared to the microporous carbon.

NMR Spectroscopy. Recent studies using solid state NMR to study carbon-organic electrolyte SC systems have shown that variations in the chemical shifts of peaks in the NMR spectra are a direct consequence of whether the electrolyte ions are adsorbed at the carbon surface or not. Specifically, the out-of-pore ions (free ions in the bulk electrolyte), the in-pore ions (free ions in micro- and mesopores), and the adsorbed ions (ions adsorbed on the charged surfaces within the pores) can be distinguished by solid-state NMR.[20,34−36] This sensitivity for probing the state of electrolyte ions makes solid state NMR an ideal technique for analyzing the selective charging behavior presented in this study. By comparing the ^1H magic angle spinning (MAS) NMR spectra of the negative electrode materials before and after charging (Figure S9), the adsorption of $EMIM^+$ ions in both charged Meso-2.0 nm and Micro-1.1 nm electrode materials was observed.[20] Notably, the charge status of the dissembled electrode materials was very stable for 20 days in the sealed Ar-filled rotor (Figure S12), making long duration ^{13}C experiments possible.

In the ^{13}C magic angle spinning (MAS) NMR spectrum, $EMIM^+$ and TMA^+ ions can be clearly distinguished, with six visible features (* shape in Figure 2c) attributed to the $EMIM^+$ ions, and one sharp feature (▲ shape in Figure 2c) being assigned to the TMA^+ ions. When the cells were charged, the two-peak broad feature at ∼80−130 ppm merged into a broad feature with a single peak, which could be related to changes in the carbon matrix during charging. A significant increase in the peak intensity of TMA^+ is observed for the charged Meso-2.0 nm carbon material relative to its uncharged state. Moreover, the intensity change of the TMA^+ feature is stronger than the changes in the $EMIM^+$ features after charging. The increased intensity of the TMA^+ peak can be explained by there being a smaller relaxation time constant for the C atom on TMA^+. This is likely due to most of the adsorbed TMA^+ ions being more closely adsorbed onto the carbon surface compared to the $EMIM^+$ ions. In contrast to these observations for the mesoporous carbon, there is no change in the relative intensity between the TMA^+ and $EMIM^+$ ions after charging for the microporous Micro-1.1 nm material. This suggests that the TMA^+ ions were not adsorbed in the micropores during charging. In short, NMR spectroscopy supports the claim that the $EMIM^+$ (^1H NMR spectra, Figures S9, S10 and S11) can be adsorbed in both, the micro- and mesopores, whereas the TMA^+ (^{13}C NMR spectra) is excluded from micropores and is only allowed to enter mesopores.

Molecular Dynamics of Ions in Charged Micro- and Mesoporous Carbons. MD simulations were also used to examine the adsorption behavior of $EMIM^+$ and TMA^+ ions in micropores (1.08 nm) and mesopores (2.16 nm). When the surface charge is −0.28 e/nm^2 (single electrode voltage = −1 V), both $EMIM^+$ and TMA^+ ions are present in the mesopores, whereas no TMA^+ ions are observed in the micropores (Figure S14). The simulation result agrees well with the NMR observation that the TMA cations selectively enter the mesopores rather than the micropores when the electrode is negatively charged. Notably, TMA^+ ions start diffusing into the micropores when larger voltages (<−2 V or surface charge beyond −0.55 e/nm^2) are applied, meaning a larger driving force is needed to adsorb TMA^+ into micropores. Moreover, both MD (Figure S15) and cDFT (Figure 1e) simulation results suggest that the TMA^+ ions are closer to the charged electrode surface, which is consistent with the NMR results.

Elimination of Ion−Ion Interactions via Solvent Addition. To understand the effects of ionic interactions on the selective charging behavior, the original ion pairing of $TMABF_4$ was eliminated through the addition of an organic solvent. Electrochemical testing was performed using a 0.3 M $TMABF_4$/propylene carbonate (PC) electrolyte with the Micro-1.1 nm carbon in a two-electrode symmetric cell. The cell using the $TMABF_4$/PC electrolyte showed near rectangular CVs at a scan rate of 20 mV/s (Figure S16a), indicating that the TMA^+ ions are able to diffuse and adsorb into the Micro-1.1 nm microporous structure. A quantum chemistry calculation combined with volume-based thermodynamics (VBT) theory[37,38] was applied to both the $EMIM^+$ and TMA^+ ions paired with the same anion, BF_4^-. Both, the lattice energy and the lattice free energy, were calculated to be higher for $TMABF_4$ than for $EMIMBF_4$ (Table S2), indicating that it is easier for $EMIM^+$ than TMA^+ to separate from BF_4^-. Therefore, it is the ion−ion interactions that result in the selectivity, instead of the geometric effect of the ions. Our cDFT calculation further suggests that the selective charging behavior of TMA^+ is dominated by the cation−anion interaction as illustrated as ionic interaction I and II in Figure 1f. Additionally, the cation−cation interactions, or steric effects (ionic interaction III) may also play a role in the ion selectivity.[17]

DOI: 10.1021/jacs.7b10693
J. Am. Chem. Soc. 2017, 139, 18681−18687

Enhanced Energy and Power of SC. The selective screening of the TMA^+ from the micropores is favorable for ion diffusion in micropores, as the entrance of the TMA^+ ions instead of $EMIM^+$ into micropores would hinder rate capability (Figure S16b). The rate capability of the Meso-2.0 nm carbon using different ionic mixture electrolytes is shown in Figure S17, with Figure 3a showing data at a current density of

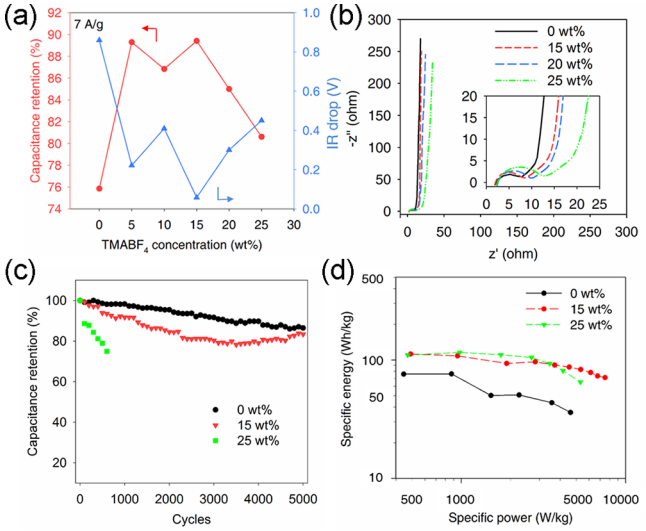

Figure 3. SC performance of Meso-2.0 nm with different $TMABF_4$ concentration. (a) Capacitance retention (capacitance at 7A/g compared to the value tested at 0.5 A/g of the same cell) and voltage drop as a function of $TMABF_4$ concentration at 7 A/g. (b) Nyquist plot; inset shows the high-frequency region. (c) Cycling stability tested at 1A/g. (d) Ragone plot.

7 A/g specifically. The capacitance retention improved and the voltage drop (or IR drop) deceased after adding $TMABF_4$ into $EMIMBF_4$, with the best performing electrolyte being the 15 wt % $TMABF_4$/$EMIMBF_4$ mixture. At 7 A/g, the capacitance retention of the 15 wt % $TMABF_4$/$EMIMBF_4$ electrolyte is 89.4%, which is much higher compared to that of the neat $EMIMBF_4$ electrolyte (75.8%). The electrolyte viscosity increases continuously as $TMABF_4$ is added into $EMIMBF_4$ (Figure S18a), whereas the conductivity first increases by 23% when the concentration of $TMABF_4$ reaches 15 wt %, but the conductivity then decreases by 7% when the concentration is further increased to 25 wt % (Figure S18b). A combination of the highest conductivity and the moderate viscosity of the 15 wt % $TMABF_4$/$EMIMBF_4$ electrolyte results in the best rate capability. Nyquist plots of Meso-2.0 nm for each electrolyte are shown in Figure 3b. The charge transfer resistance increases from 8 to 10 ohms when the concentration of the $TMABF_4$ increases from 0 to 20 wt %. Further increases in the $TMABF_4$ concentration lead to continued increases in resistance, with a charge transfer resistance of 14 ohms at the $TMABF_4$ concentration of 25 wt %. The impedance results are consistent with the rate handling performance shown before, where the best result was achieved when the concentration of $TMABF_4$ was 15 wt %.

The SC of Meso-2.0 nm using 15 wt % $TMABF_4$/$EMIMBF_4$ electrolyte showed good cycling stability with ca. 84% capacitance retention after 5000 cycles (Figure 3c), slightly worse than that of the neat $EMIMBF_4$ electrolyte (86%). The increase in capacitance retention starting at cycle 3000 is small (a few percent), so this phenomenon is considered to be within error and not a special property of the mixed electrolyte. It is also clearly shown that the cell using 25 wt % $TMABF_4$/$EMIMBF_4$ electrolyte has significantly worse cycling stability when compared to the 15. wt % electrolyte. The decline in cycling stability could be attributed to side reactions that are apparent from the distorted GCD curve of the 25 wt % electrolyte (Figure S5). It should be noted that the cyclability tests performed here were used strictly for evaluating the behavior of the mixed electrolytes relative to the neat $EMIMBF_4$ electrolyte. Systematic optimization of the electrolyte composition and behavior is being pursued separately. The Ragone plot in Figure 3d shows that the use of the 15 wt % $TMABF_4$/$EMIMBF_4$ electrolyte resulted in a 43% increase in maximum energy compared to the neat $EMIMBF_4$ electrolyte. For further comparison, the neat $EMIMBF_4$ electrolyte had 50% energy retention at a power of 4700 W/kg, while the 15 wt % $TMABF_4$/$EMIMBF_4$ electrolyte had an energy retention of 68% at a power of 7500 W/kg. Therefore, the addition of the $TMABF_4$ into $EMIMBF_4$ results in increased energy density without sacrificing power. The results shown here suggest that suitable modifications to the selectivity of ion adsorption at electrode surfaces has the potential to increase the energy density of energy storage systems operating on the physisorption of charge carriers without negatively impacting the power density.

CONCLUSION

In this study, in-cell charging selectivity was demonstrated through balancing the interactions between the charge carrying ions of the electrolyte and the interactions of the electrolyte with porous structures of the electrode materials. The selective sieving of TMA^+ ions from micropores eliminates the slow ion transport of TMA^+ ions that would occur in micropores. Meanwhile, TMA^+ ions can freely enter mesopores and enhance the mesopore capacitance by increasing the number density of adsorbed cations at the electrode surface by introducing strong cation−cation interactions between the $EMIM^+$ and TMA^+ ions. By using this method, the energy density of the SC was increased without sacrificing power density. The results shown here represent a strategy for designing selective charging behavior in an ionic mixture electrolyte by utilizing differences in ionic interactions. Furthermore, the realization of selective charging behavior in one SC system shown here opens the possibility for exploring similar energy management strategies in other energy storage systems, with the goal of moving toward more robust and efficient energy storage devices.

METHODS

Materials. Except for the activated carbon YP-50F, all of the carbon materials in this study were synthesized in the lab, with detailed synthesis methods described in the Supporting Information (S1.1). 0, 5, 10, 15, 20, 25 wt % of the $TMABF_4$ salt was mixed with the neat $EMIMBF_4$ by stirring followed by sonication for 1 h before use.

Material Characterization. N_2 sorption (−196 °C) isotherms were recorded on a Micromeritics Tristar II 3020 instrument. The samples were degassed at 200 °C for 12 h under turbomolecular vacuum pumping prior to the gas adsorption measurements. The general morphology of all carbon materials was characterized by scanning electron microscopy (STEM, Hitachi S-5500). The conductivity of the electrolytes was tested using a EP357 conductivity isoPod with an ET915 miniature Dip-In Conductivity Electrode. Viscosity tests were performed using a Haake Mars III rheometer and recorded at a stirring speed of 1000 rad/min. The NMR experiments were performed at 11.7 T (500 MHz proton resonance frequency) with a

DOI: 10.1021/jacs.7b10693
J. Am. Chem. Soc. 2017, 139, 18681−18687

4.0 mm double resonance MAS probehead at room temperature using a Bruker Avance III spectrometer. All ^{1}H and ^{13}C spectra were acquired using single pulse excitations. Proton decoupling was applied in the ^{13}C experiments (for more details, see Supporting Information Part S4).

Carbon Electrodes and Supercapacitor Cells. All carbon materials were mixed with polytetrafluoroethylene binder (5 wt %) (Sigma-Aldrich, 60 wt % dispersion in water) in ethanol. The mixed slurry was kneaded and rolled into a free-standing film before being cut into disk shaped electrodes with diameters of 8 mm and mass of 2.5−4 mg. The electrodes were dried under vacuum for at least 12 h at 200 °C prior to use. The SC cells were prepared by pressing the electrode disks onto carbon-coated aluminum foil in a glovebox with controlled atmosphere (O_2 < 0.1 ppm and H_2O < 0.1 ppm, Vacuum Technologies Inc.). Two electrodes with the same mass were separated by a 25 μm thick polypropylene membrane (Celgard 3501), with about 20 μL of the electrolyte on each side of the membrane. Following assembly, the cells were clamped and sealed inside a polyethylene terephthalate bag and stabilized overnight before electrochemical testing.

Electrochemical Measurements. The GCD tests, rate capability, and cycling experiments were carried out using a MTI 8-channel battery analyzer, whereas the CVs and impedance analysis was done using a Princeton VersaSTAT potentiostat analyzer. The gravimetric capacitance of the single electrodes was calculated from the GCD discharge branch based on: $C_{sp,electrode} = \frac{4I\cdot\Delta t}{m_{total}\cdot V_{cell}}$, where I is the constant discharge current, m_{total} is the total mass of the active materials on two electrodes, Δt is the discharge time and V_{cell} is the voltage change of cell during the discharge process (excluding the voltage drop at the beginning of the discharge). CVs were also used to calculate the capacitance based on: $C_{sp,electrode} = \frac{4\int it}{m_{total}\cdot V_{cell}}$, and the i is the current density changed by time.

The specific energy and the average power were then estimated based on the equations: $E_{sp,cell} = \frac{1}{8}C_{sp,electrode}\cdot {V_{cell}}^2$ and $P_{sp,cell,ave} = E_{sp,cell}/\Delta t$.

■ ASSOCIATED CONTENT

Supporting Information

The Supporting Information is available free of charge on the ACS Publications website at DOI: 10.1021/jacs.7b10693.

Material synthesis and characterization, electrochemical characterization, DFT simulation results, solid state NMR results, MD simulation results and additional information related to the power property of supercapacitor (PDF)

■ AUTHOR INFORMATION

Corresponding Authors

*gogotsi@drexel.edu
*de.chen@ntnu.no

ORCID

Xuehang Wang: 0000-0002-8984-6162
Aleksandar Yordanov Mehandzhiyski: 0000-0001-5671-4545
Bjørnar Arstad: 0000-0003-0398-786X
Ziqi Tian: 0000-0001-5667-597X
De-en Jiang: 0000-0001-5167-0731
Jianzhong Wu: 0000-0002-4582-5941
Yury Gogotsi: 0000-0001-9423-4032
De Chen: 0000-0002-5609-5825

Notes

The authors declare no competing financial interest.

■ ACKNOWLEDGMENTS

The MD simulation, solid-state NMR and part of electrochemical analysis were funded by the Research Council of Norway via project 10388902 and NorFab 197411/V30. The research of DFT modeling and part of electrochemical analysis was sponsored by the Fluid Interface Reactions, Structures, and Transport (FIRST) Center, an Energy Frontier Research Center (EFRC) funded by the U.S. Department of Energy, Office of Science, and Office of Basic Energy Sciences. The cDFT calculations were performed at the National Energy Research Scientific Computing Center (NERSC). We thank David J. Wesolowski (Oak Ridge National Laboratory) for helpful discussions. We also thank Kun Liu (UCR), Zhongde Dai (NTNU) and Torun Margareta Melø (NTNU) for some material characterization.

■ REFERENCES

(1) Simon, P.; Gogotsi, Y. *Nat. Mater.* **2008**, *7* (11), 845−854.
(2) Gogotsi, Y.; Simon, P. *Science* **2011**, *334* (6058), 917−918.
(3) Salanne, M.; Rotenberg, B.; Naoi, K.; Kaneko, K.; Taberna, P.-L.; Grey, C. P.; Dunn, B.; Simon, P. *Nat. Energy* **2016**, *1*, 16070.
(4) Van Aken, K. L.; Beidaghi, M.; Gogotsi, Y. *Angew. Chem., Int. Ed.* **2015**, *54* (16), 4806−4809.
(5) Armand, M.; Endres, F.; MacFarlane, D. R.; Ohno, H.; Scrosati, B. *Nat. Mater.* **2009**, *8* (8), 621−629.
(6) Chmiola, J.; Yushin, G.; Gogotsi, Y.; Portet, C.; Simon, P.; Taberna, P.-L. *Science* **2006**, *313* (5794), 1760−1763.
(7) Largeot, C.; Portet, C.; Chmiola, J.; Taberna, P.-L.; Gogotsi, Y.; Simon, P. *J. Am. Chem. Soc.* **2008**, *130* (9), 2730−2731.
(8) Wang, X.; Zhou, H.; Sheridan, E.; Walmsley, J. C.; Ren, D.; Chen, D. *Energy Environ. Sci.* **2016**, *9* (1), 232−239.
(9) Béguin, F.; Presser, V.; Balducci, A.; Frackowiak, E. *Adv. Mater.* **2014**, *26* (14), 2219−2251.
(10) Lin, R.; Huang, P.; Segalini, J.; Largeot, C.; Taberna, P.-L.; Chmiola, J.; Gogotsi, Y.; Simon, P. *Electrochim. Acta* **2009**, *54* (27), 7025−7032.
(11) Richey, F. W.; Dyatkin, B.; Gogotsi, Y.; Elabd, Y. A. *J. Am. Chem. Soc.* **2013**, *135* (34), 12818−12826.
(12) Péan, C.; Merlet, C.; Rotenberg, B.; Madden, P. A.; Taberna, P.-L.; Daffos, B.; Salanne, M.; Simon, P. *ACS Nano* **2014**, *8* (2), 1576−1583.
(13) Forse, A. C.; Griffin, J. M.; Merlet, C.; Carretero-Gonzalez, J.; Raji, A.-R. O.; Trease, N. M.; Grey, C. P. *Nat. Energy* **2017**, *2*, 16216.
(14) Pean, C.; Daffos, B.; Rotenberg, B.; Levitz, P.; Haefele, M.; Taberna, P.-L.; Simon, P.; Salanne, M. *J. Am. Chem. Soc.* **2015**, *137* (39), 12627−12632.
(15) Wang, X.; Zhou, H.; Lou, F.; Li, Y.; Buan, M. E.; Duan, X.; Walmsley, J. C.; Sheridan, E.; Chen, D. *ChemSusChem* **2016**, *9* (21), 3093−3101.
(16) Kornyshev, A. A. *J. Phys. Chem. B* **2007**, *111* (20), 5545−5557.
(17) Segalini, J.; Iwama, E.; Taberna, P.-L.; Gogotsi, Y.; Simon, P. *Electrochem. Commun.* **2012**, *15* (1), 63−65.
(18) Merlet, C.; Rotenberg, B.; Madden, P. A.; Taberna, P.-L.; Simon, P.; Gogotsi, Y.; Salanne, M. *Nat. Mater.* **2012**, *11* (4), 306−310.
(19) Tsai, W.-Y.; Taberna, P.-L.; Simon, P. *J. Am. Chem. Soc.* **2014**, *136* (24), 8722−8728.
(20) Forse, A. C.; Griffin, J. M.; Merlet, C. l.; Bayley, P. M.; Wang, H.; Simon, P.; Grey, C. P. *J. Am. Chem. Soc.* **2015**, *137* (22), 7231.
(21) Merlet, C.; Péan, C.; Rotenberg, B.; Madden, P. A.; Daffos, B.; Taberna, P.-L.; Simon, P.; Salanne, M. *Nat. Commun.* **2013**, *4*, 2701.
(22) Chmiola, J.; Largeot, C.; Taberna, P. L.; Simon, P.; Gogotsi, Y. *Angew. Chem.* **2008**, *120* (18), 3440−3443.
(23) He, Y.; Qiao, R.; Vatamanu, J.; Borodin, O.; Bedrov, D.; Huang, J.; Sumpter, B. G. *J. Phys. Chem. Lett.* **2016**, *7* (1), 36−42.
(24) Lian, C.; Liu, H.; Henderson, D.; Wu, J. *J. Phys.: Condens. Matter* **2016**, *28* (41), 414005.
(25) Forse, A. C.; Merlet, C.; Griffin, J. M.; Grey, C. P. *J. Am. Chem. Soc.* **2016**, *138* (18), 5731−5744.
(26) Ye, C.; Shreeve, J. n. M. *J. Phys. Chem. A* **2007**, *111* (8), 1456−1461.

DOI: 10.1021/jacs.7b10693
J. Am. Chem. Soc. 2017, 139, 18681−18687

(27) Welton, T. *Chem. Rev.* **1999**, *99* (8), 2071−2084.
(28) Ania, C.; Pernak, J.; Stefaniak, F.; Raymundo-Piñero, E.; Béguin, F. *Carbon* **2006**, *44* (14), 3126−3130.
(29) Lin, R.; Taberna, P.-L.; Fantini, S.; Presser, V.; Pérez, C. R.; Malbosc, F.; Rupesinghe, N. L.; Teo, K. B.; Gogotsi, Y.; Simon, P. *J. Phys. Chem. Lett.* **2011**, *2* (19), 2396−2401.
(30) Tsai, W.-Y.; Lin, R.; Murali, S.; Zhang, L. L.; McDonough, J. K.; Ruoff, R. S.; Taberna, P.-L.; Gogotsi, Y.; Simon, P. *Nano Energy* **2013**, *2* (3), 403−411.
(31) Mecozzi, S.; West, A. P.; Dougherty, D. A. *J. Am. Chem. Soc.* **1996**, *118* (9), 2307−2308.
(32) Matthews, R. P.; Welton, T.; Hunt, P. A. *Phys. Chem. Chem. Phys.* **2014**, *16* (7), 3238−3253.
(33) Gallivan, J. P.; Dougherty, D. A. *J. Am. Chem. Soc.* **2000**, *122* (5), 870−874.
(34) Deschamps, M.; Gilbert, E.; Azais, P.; Raymundo-Piñero, E.; Ammar, M. R.; Simon, P.; Massiot, D.; Béguin, F. *Nat. Mater.* **2013**, *12* (4), 351−358.
(35) Griffin, J. M.; Forse, A. C.; Tsai, W.-Y.; Taberna, P.-L.; Simon, P.; Grey, C. P. *Nat. Mater.* **2015**, *14* (8), 812−819.
(36) Wang, H.; Köster, T. K.-J.; Trease, N. M.; Segalini, J.; Taberna, P.-L.; Simon, P.; Gogotsi, Y.; Grey, C. P. *J. Am. Chem. Soc.* **2011**, *133* (48), 19270−19273.
(37) Glasser, L.; Jenkins, H. D. B. *Chem. Soc. Rev.* **2005**, *34* (10), 866−874.
(38) Krossing, I.; Slattery, J. M.; Daguenet, C.; Dyson, P. J.; Oleinikova, A.; Weingärtner, H. *J. Am. Chem. Soc.* **2006**, *128* (41), 13427−13434.

DOI: 10.1021/jacs.7b10693
J. Am. Chem. Soc. 2017, 139, 18681−18687